

Evolutionary deformation toward the elastic limit by a magnetic field confined in the neutron-star crust

YASUFUMI KOJIMA,¹ SHOTA KISAKA,¹ AND KOTARO FUJISAWA²

¹ *Department of Physics, Graduate School of Advanced Science and Engineering,
Hiroshima University, Higashi-Hiroshima, Hiroshima 739-8526, Japan*

² *Department of Physics, Graduate School of Science, University of Tokyo, Bunkyo-ku, Tokyo 113-0033, Japan*

(Dated: March 7, 2023)

ABSTRACT

Occasional energetic outbursts and anomalous X-ray luminosities are expected to be powered by the strong magnetic field in a neutron star. For a very strong magnetic field, elastic deformation becomes excessively large such that it leads to crustal failure. We studied the evolutionary process driven by the Hall drift for a magnetic field confined inside the crust. Assuming that the elastic force acts against the Lorentz force, we examined the duration of the elastic regime and maximum elastic energy stored before the critical state. The breakup time was longer than that required for extending the field to the exterior, because the tangential components of the Lorentz force vanished in the fragile surface region. The conversion of large magnetic energy, confined to the interior, into Joule heat is considered to explain the power for central compact objects. This process can function without reaching its elastic limit, unless the magnetic energy exceeds 2×10^{47} erg, which requires an average field strength of 2×10^{15} G. Thus, the strong magnetic field hidden in the crust is unlikely to cause outbursts. Furthermore, the magnetic field configuration can discriminate between central compact objects and magnetars.

Keywords: Neutron stars; Compact objects; Magnetars; High-energy astrophysics

1. INTRODUCTION

The magnetic field strength on a neutron-star surface is typically approximately 10^{12} G. However, there are two peculiar classes whose field strengths significantly deviate from the average. They exhibit unusual activities, with their energy considered to be supplied by an intense magnetic field. Magnetars, except for a few sources, have a strong dipole field $\geq 10^{14}$ G and exhibit energetic outbursts or flares. The X-ray luminosity is very bright in the range 10^{32} – 10^{36} ergs⁻¹, which exceeds the spin-down luminosity for most sources, in contrast to normal pulsars (Turolla et al. 2015; Kaspi & Beloborodov 2017; Enoto et al. 2019; Esposito et al. 2021, for review).

Central compact objects (CCOs) located at the centers of supernova remnants are X-ray sources with luminosity $\sim 10^{32}$ – 10^{34} ergs⁻¹. A few CCOs show pulsations; hence, the magnetic dipole field is estimated to be $\sim 10^{10}$ – 10^{11} G, (Gotthelf et al. 2013). Their X-ray luminosities are comparable to those of quiescent magnetars (Kaspi & Beloborodov 2017), and exceed the kinetic energy loss. To explain the X-ray luminosity, CCOs are considered to have an intense magnetic field $\sim 10^{14}$ G inside neutron stars, although the surface field is weak. Strong fields near the surface or inside the crust may explain the nonuniform temperature of PSR J0822-4300 in Puppis A (Gotthelf et al. 2010) and large pulse fraction of PSR J1852+0040 in Kes 79 (Shabaltas & Lai 2012). Most of the magnetic field in CCOs is considered to be buried by the fallback of the supernova material (Ho 2011; Viganò & Pons 2012). Numerical simulations can be used to solve the field geometry of the proto-neutron star (see, e.g. Matsumoto et al. 2022, for recent development).

Such a strong field $\sim 10^{14}$ G is crucial for studying magnetized neutron stars. The Lorentz force is comparable in magnitude to the elastic force in the crust. However, only static magneto-elastic equilibria of the crust have been studied thus far (Kojima et al. 2021, 2022; Fujisawa et al. 2023). These studies demonstrated that neutron star models with strong magnetic fields are possible owing to the elasticity of the crust. A magnetic field configuration was assumed in these studies. However, it is unclear whether a sufficient range of magnetic field was covered or not.

Herein, we consider the effect of the elastic force in the equilibria of magnetized neutron stars from a different perspective. In other words, we examined the process toward the elastic limit according to magnetic field evolution. Suppose that the magnetized crust settles in the force balance at a particular time. However, the magnetic field is not fixed and evolves on a secular timescale. Thus, elastic displacement is induced from the initial position to balance the Lorentz force according to field evolution. Simultaneously, shear stress in the crust gradually accumulates and reaches a critical limit. Beyond this threshold, the crust cracks (Duncan & Thompson 1992; Thompson & Duncan 1995, for a seminal paper) or responds plastically. Two possibilities are discussed owing to the lack of a sufficient understanding of the material properties. A sudden crust breaking can produce a magnetar outburst and/or a fast radio burst (Li et al. 2016; Baiko & Chugunov 2018; Suvorov & Kokkotas 2019). Second, plastic flow beyond a critical point is crucial for the long-term evolution (Lander 2016), and a coupled system between the flow and the magnetic field was numerically solved (Lander & Gourgouliatos 2019; Kojima & Suzuki 2020; Gourgouliatos & Lander 2021). Therefore, it is important to explore the timescale up to the critical limit, and the elastic energy deposited during the evolution.

In this study, we assumed that the stellar structure is always barotropic. The initial state of evolution is described by magneto-hydrodynamic (MHD) equilibrium without the elastic force. This equilibrium does not involve electrons. (Gourgouliatos et al. 2013; Gourgouliatos & Cumming 2014); thus, the magnetic field tends toward Hall equilibrium on a secular timescale. The Hall–drift timescale, an important indicator in the evolution, becomes shorter as the magnetic field strength increases. Thus, this study is relevant to neutron star crusts with strong magnetic fields.

A previous study considered the evolution of a magnetic field that extended from the crust to the exterior (Kojima 2022, referred to as Paper I). However, the toroidal component of the magnetic field was ignored. It is important to examine the evolution of different magnetic field geometries. The broad classification is based on whether the field is confined inside the crust or spreads out to the magnetosphere. This possibility is schematically illustrated in Figure 1. For simplicity, we assume that the field is purely dipolar and is expelled from the neutron–star core. The extended case shown in Figure 1-a (left panel) corresponds to the magnetar model considered in Paper I. The toroidal component of the magnetic field cannot emerge in an exterior vacuum; it is confined inside a loop in the meridional plane for the poloidal component, as shown in Figure 1-b (middle panel) and 1-c (right panel). The toroidal magnetic energy potentially increases as the loop region expands. In contrast to Paper I, this study considered the entirely confined case, shown in Figure 1-c. Both the toroidal and poloidal components are confined in the crust. The magnetic field geometry can be applied to that of CCOs.

The remainder of this paper is organized as follows. The models and equations used in this study are discussed in Section 2. We calculated the quasi-stationary evolution of the shear strain induced by the Hall drift of a magnetic field. We estimated the critical time beyond which the elastic equilibrium was no longer possible as well as the elastic energy during evolution. The numerical results are presented in Section 3. Finally, our conclusions are presented in Section 4.

2. MATHEMATICAL FORMULATION

2.1. Barotropic Equilibrium in Crust

Our consideration was limited to the inner crust of a neutron star, where the mass density ranges from $\rho_c = 1.4 \times 10^{14}$ g cm⁻³ at the core–crust boundary r_c to the neutron drip density $\rho_1 = 4 \times 10^{11}$ g cm⁻³ at $R = 12$ km. We ignored the outer crust and treated the exterior region of $r > R$ as a vacuum. The crust thickness $\Delta r \equiv R - r_c$ was assumed to be $\Delta r/R = 0.05$ and $\Delta r = 0.6$ km. The spatial density profile in $r_c \leq r \leq R$ is approximated as (Lander & Gourgouliatos 2019)

$$\hat{\rho} \equiv \frac{\rho}{\rho_c} = \left[1 - \left(1 - \left(\frac{\rho_1}{\rho_c} \right)^{1/2} \right) \left(\frac{r - r_c}{\Delta r} \right) \right]^2. \quad (1)$$

We consider the equilibrium in the crust. Under the Newtonian approximation, static force balance between the pressure P , gravity, and Lorentz force is expressed as

$$-\frac{1}{\rho} \vec{\nabla} P - \vec{\nabla} \Phi_g + \frac{1}{c\rho} \vec{j} \times \vec{B} = 0, \quad (2)$$

where Φ_g is the gravitational potential including the centrifugal term. We assume a barotropic distribution $P = P(\rho)$, and the sum of the first two terms in Equation (2), is expressed as $-\vec{\nabla} \Phi_{\text{eff}}$. The third term has a magnitude

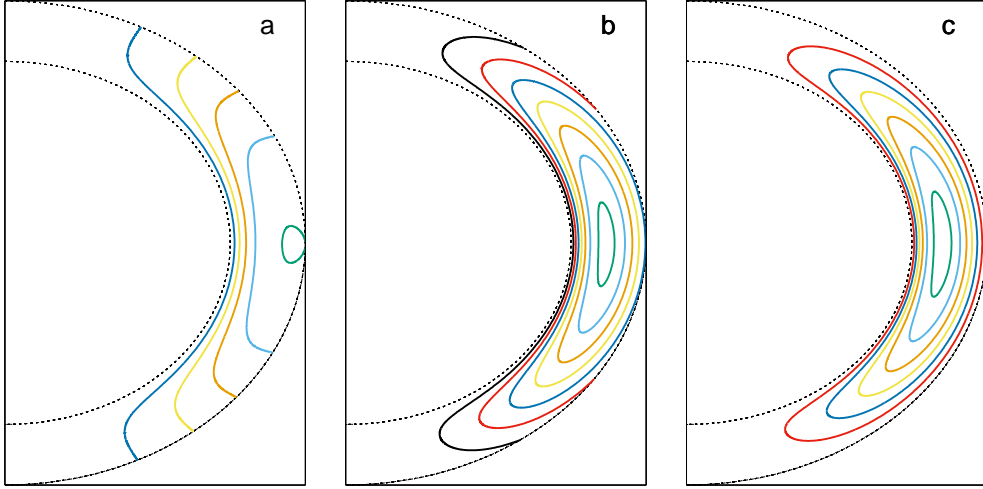


Figure 1. Magnetic field geometry in crust. Contours of magnetic function $\Psi(r, \theta)$ for a poloidal field are demonstrated. From the left to right panels, the field is more confined, and the toroidal component is also involved in the interior.

$\sim 10^{-7}(B/10^{14}\text{G})^2$ times smaller than those for the first and second terms. The deviation due to the Lorentz force is sufficiently small to be treated as a perturbation of the background equilibrium.

We assumed an axial symmetry for the magnetic-field configuration. The poloidal and toroidal components of the magnetic field are expressed by two functions, Ψ and S , respectively, as follows:

$$\vec{B} = \vec{\nabla} \times \left(\frac{\Psi}{\varpi} \vec{e}_\phi \right) + \frac{S}{\varpi} \vec{e}_\phi, \quad (3)$$

where $\varpi = r \sin \theta$ is the cylindrical radius and \vec{e}_ϕ is the azimuthal unit vector in (r, θ, ϕ) coordinates. For barotropic equilibrium, the current function S should be a function of Ψ , and the azimuthal component j_ϕ of the electric current is described in the form (e.g., Tomimura & Eriguchi 2005)

$$\frac{4\pi j_\phi}{c} = \rho\varpi \frac{dK}{d\Psi} + \frac{S}{\varpi} \frac{dS}{d\Psi}, \quad (4)$$

where K denotes a function of Ψ . Further, the acceleration \vec{a} owing to the Lorentz force is reduced to

$$\vec{a} \equiv \frac{1}{c\rho} \vec{j} \times \vec{B} = \frac{1}{4\pi} \vec{\nabla} K. \quad (5)$$

Thus, the force balance in Equation (2) is described by the gradient terms of scalar functions.

We adopted a simple linear function of Ψ for $K(\Psi)$ and $S(\Psi)$. $K = K_0\Psi$ and $S = \kappa\Psi$, where K_0 and κ are constant. For the dipole field, function Ψ is expressed using the Legendre polynomial of $l = 1$, that is, $\Psi = g(r) \sin^2 \theta$. After the

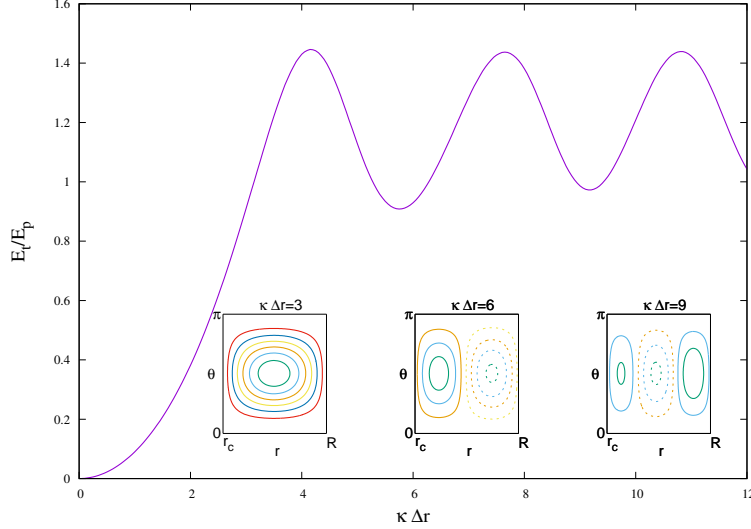


Figure 2. Energy ratio as a function of $\kappa\Delta r$. Contours of Ψ in the $r - \theta$ plane for $\kappa\Delta r = 3, 6$, and 9 are shown. Contours with negative values of Ψ are indicated by dotted lines.

decomposition of the angular part, the azimuthal component of the Ampère law is reduced to

$$g'' - \frac{2g}{r^2} + \kappa^2 g = -K_0 \rho r^2, \quad (6)$$

where prime ' denotes a derivative with respect to r . We consider a magnetic field confined in the crust such that the radial function g is obtained by solving Equation (6) using boundary conditions $g(r_c) = g(R) = 0$. The solutions for Equation (6) without the source term are obtained using spherical Bessel functions. A homogeneous solution satisfies the following boundary conditions: only for specific values, $\kappa\Delta r \approx n\pi$ ($n = 1, 2, \dots$). This solution corresponds to a force-free case $\vec{j} \times \vec{B} = 0$, that is, $K_0 = 0$ in Equation (5).

The constant K_0 determines the overall magnetic field strength, whereas κ determines the ratio of the poloidal and toroidal components. The dipolar magnetic field considered in Paper I is purely poloidal ($\kappa = 0$) and extends to the exterior vacuum. The magnetic energy E_p stored inside the crust is expressed as $E_p = 3.8B_0^2 R^3$, using field strength B_0 at the surface. When studying different models confined to the crust, we always fixed the poloidal magnetic energy as $E_p = 3.8B_0^2 R^3$. The average strength is approximated as $12B_0$, whereas the normalization B_0 also fixes K_0 for each model.

Figure 2 shows the energy ratio of toroidal components E_t to poloidal components E_p as functions of $\kappa\Delta r$. A similar result was obtained for the magnetic field confined in the whole star (Fujisawa & Eriguchi 2013). The ratio increased with $\kappa\Delta r$ and reached a maximum ~ 1.4 . With further increase, the ratio oscillated between the minimum ~ 1 and the maximum ~ 1.4 . Further, the spatial structure of the magnetic function Ψ changed continuously; the radial nodes increased with $\kappa\Delta r$ as shown in Figure 2. Node number n is approximated as $n \approx \kappa\Delta r/\pi$.

2.2. Magnetic-Field Evolution

The force balance expressed as Equation (2) is not fixed on a secular timescale because the Lorentz force $\vec{j} \times \vec{B}$ gradually changes owing to magnetic field evolution. The evolution of the crustal magnetic field was governed by the following induction equation:

$$\frac{\partial}{\partial t} \vec{B} = -\vec{\nabla} \times \left[\frac{1}{en_e} \vec{j} \times \vec{B} + \frac{c}{\sigma_e} \vec{j} \right], \quad (7)$$

where n_e is the electron number density and σ_e is the electrical conductivity. The first term in Equation (7) represents the Hall drift, and the second term represents the magnetic decay due to ohmic dissipation. The timescales associated

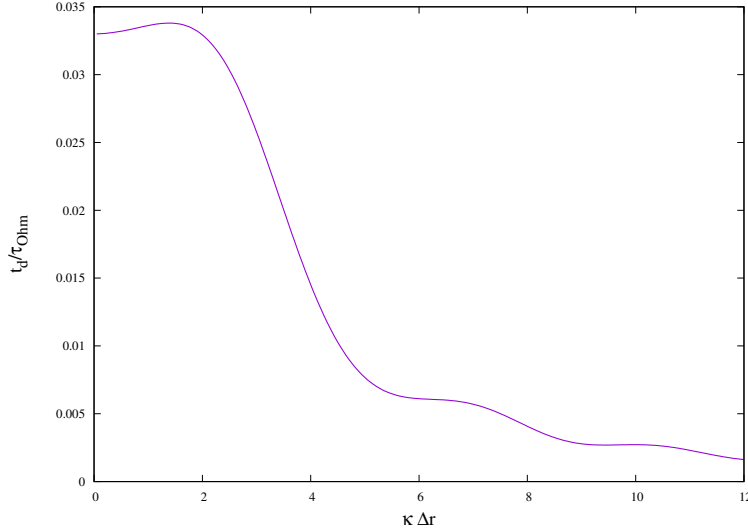


Figure 3. Magnetic decay time t_d/τ_{Ohm} as a function of $\kappa\Delta r$.

with these processes are estimated as

$$\tau_{\text{H}} = \frac{4\pi en_{\text{ec}}(\Delta r)^2}{cB_0} = 7.9 \times 10^5 \left(\frac{B_0}{10^{14}\text{G}} \right)^{-1} \text{ yr}, \quad (8)$$

$$\tau_{\text{Ohm}} = \frac{4\pi\sigma_{\text{ec}}(\Delta r)^2}{c^2} = 2.1 \times 10^6 \text{ yr}, \quad (9)$$

where B_0 denotes the normalization of the magnetic field strength, and crust thickness $\Delta r = 0.05R = 0.6\text{km}$ is used. In Equations (8) and (9), we used the maximum values for n_e and σ_e , that is, the values at the core–crust boundary.

$$n_{\text{ec}} = 3.4 \times 10^{36} \text{ cm}^{-3}, \quad \sigma_{\text{ec}} = 1.5 \times 10^{24} \text{ s}^{-1}. \quad (10)$$

The actual timescales may be smaller than those obtained using Equations (8) and (9), owing to the spatial dependence of n_e , σ_e , \vec{B} , and \vec{j} .

Here, we estimate the magnetic decay for the confined models considered in the previous subsection, using numerical calculations. The energy decay time t_d is defined as

$$t_d \equiv 2E_{\text{B}} \left(\int \frac{j^2}{\sigma_e} dV \right)^{-1}, \quad (11)$$

where E_{B} denotes the total magnetic energy. $E_{\text{B}} = E_{\text{p}} + E_{\text{t}}$. The field strength B decreased by approximately $B \propto \exp(-t/t_d)$. Further, the magnetic energy ($E_{\text{B}} \propto B^2 \propto \exp(-2t/t_d)$) was dissipated by one order in the period $(0.5 \ln 10) \times t_d \approx 1.2t_d$. We calculated t_d using an analytical model for the electric conductivity distribution (Lander & Gourgouliatos 2019);

$$n_e = n_{\text{ec}} \left(0.44\hat{\rho}^{2/3} + 0.56\hat{\rho}^2 \right), \quad \sigma_e = \sigma_{\text{ec}} \left(\frac{n_e}{n_{\text{ec}}} \right)^{2/3}, \quad (12)$$

where $\hat{\rho} = \rho/\rho_c$ is expressed as Equation (1).

Figure 3 shows the results for a confined field. The small ratio $t_d/\tau_{\text{Ohm}} \sim 10^{-2}$ originates largely from the choice of the maximum value of electric conductivity σ_{ec} in Equation (9). Thus, we found that the dissipation time is of the following order: $3 \times (10^{-3} - 10^{-2}) \times \tau_{\text{Ohm}} \sim 6 \times 10^3 - 6 \times 10^4 \text{ yr}$.

During this period, the magnetic energy was converted to heat at a rate of

$$\dot{Q} = \frac{2E_{\text{B}}}{t_d} \approx 7 \times (10^{34} - 10^{35}) \times \left(\frac{B_0}{10^{14}\text{G}} \right)^2 \text{ erg s}^{-1}. \quad (13)$$

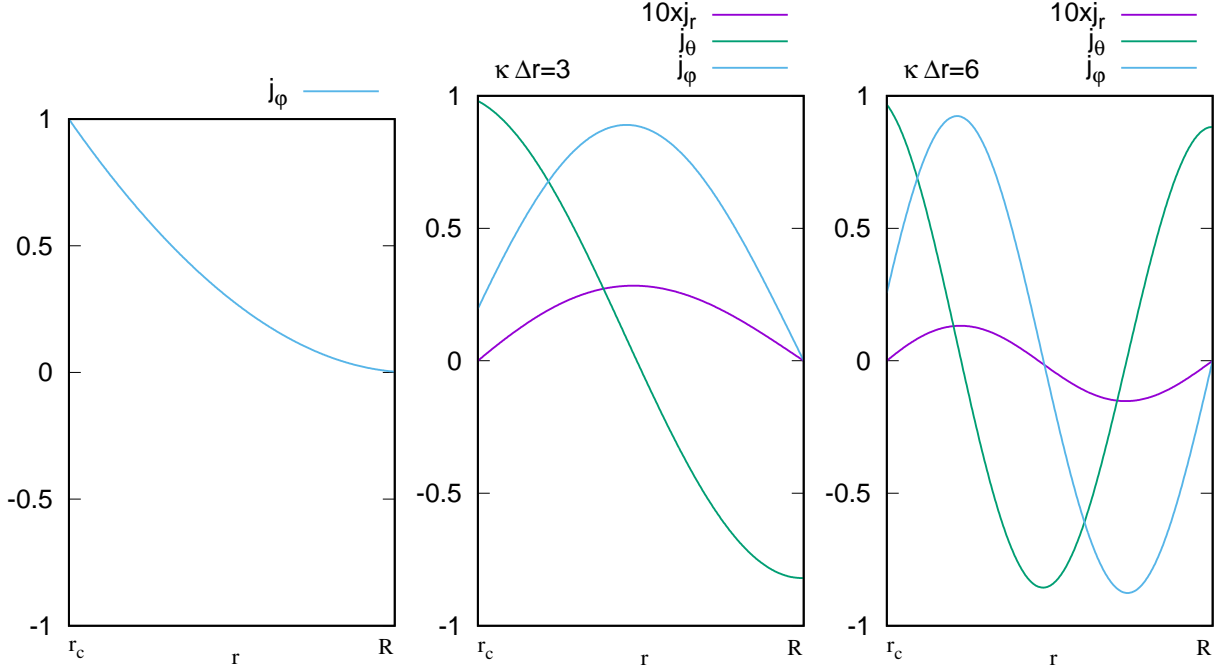


Figure 4. Electric currents in crust. Radial functions ($j_r/\cos\theta, j_\theta/\sin\theta, j_\phi/\sin\theta$) are shown for three models. The left to right panels correspond to the extending field, confined field with $\kappa\Delta r = 3$, and confined field with $\kappa\Delta r = 6$, respectively. The amplitudes are normalized by the maximum of $|\vec{j}|$. The radial component j_r for the confined models is small, typically $j_r \sim (\Delta r/R) \times j_\theta = j_\theta/20$, such that j_r in the figures is multiplied by a factor of 10.

This power is sufficient to supply the X-ray luminosity of CCO $\sim 1.5 \times 10^{32} - 10^{34}$ erg s $^{-1}$.

To study the effect of the magnetic geometry, we also compared the dissipation timescale for extending the field to the exterior, where $t_d/\tau_{\text{Ohm}} = 5.9 \times 10^{-2}$. This value was larger than that for the confined field. Among the confined field models, t_d/τ_{Ohm} decreased slightly with an increase in $\kappa\Delta r$. As the radial number increased, the typical length and the dissipation time decreased. The stepwise curve of t_d/τ_{Ohm} in Figure 3 corresponds to this transition.

We considered the electric current distribution. The angular dependence is expressed as $j_r \propto \cos\theta$, $j_\theta \propto \sin\theta$, and $j_\phi \propto \sin\theta$ because the magnetic field is dipolar ($l = 1$). Figure 4 shows the radial functions of the electric currents for the three models. The current for the extended model in the left panel is the maximum at the inner boundary $r = r_c$ and decreases radially. However, for the confined models, we found that j_θ is large at the surface, while $j_r = j_\phi = 0$. Component $j_\theta \neq 0$ near the surface decayed significantly because of the low electric conductivity, thereby resulting in a larger value of t_d/τ_{Ohm} .

2.3. Hall-drift Evolution

The Hall-Ohmic equation (7) was studied for axially symmetric models (Pons & Geppert 2007; Kojima & Kisaka 2012; Viganò et al. 2013; Gourgouliatos et al. 2013; Gourgouliatos & Cumming 2014; Viganò et al. 2021), and for 3D models (Wood & Hollerbach 2015; Viganò et al. 2019; De Grandis et al. 2020; Gourgouliatos et al. 2020; Igoshev et al. 2021). Here, we limit the evolution to the early phase such that the calculation is simplified.

By comparing the two timescales expressed as Equations (8) and (9), it was revealed that the magnetic field evolution is governed by Hall drift in the strong-magnetic-field regime. In the range $t < t_d \sim 10^4$ y, we may neglect Ohmic decay in Equation (7) and the induction equation is reduced to

$$\frac{\partial}{\partial t} \vec{B} = -\vec{\nabla} \times \left[\frac{1}{en_e} \vec{j} \times \vec{B} \right] = -\vec{\nabla} \chi \times \vec{a} - \chi \vec{\nabla} \times \vec{a}, \quad (14)$$

where

$$\chi \equiv \frac{c\rho}{en_e} = \frac{4\pi\rho_c(\Delta r)^2}{\tau_H B_0} \hat{\chi}. \quad (15)$$

In Equation (15), $\hat{\chi}$ is the non-dimensional ratio of mass density to electron number density, and is approximated by a smooth analytic function to fit the data given by (Douchin & Haensel 2001, Paper I),

$$\hat{\chi} = \frac{\hat{\rho}^{1/2}}{0.32 + 0.66\hat{\rho}}, \quad (16)$$

where $\hat{\rho} = \rho/\rho_c$ is expressed as Equation (1). The second term in Equation (14) vanishes at $t = 0$ owing to Equation (5), because barotropic equilibrium is assumed. Moreover, the first term vanishes when χ is constant. In other words, the barotropic MHD equilibrium is the Hall equilibrium for electrons (Gourgouliatos et al. 2013). We consider the magnetic-field evolution driven by nonuniform distribution of χ . The early phase of barotropic MHD equilibrium is governed by

$$\frac{\partial}{\partial t} \vec{B} = -\chi' a_\theta \vec{e}_\phi. \quad (17)$$

The azimuthal component, B_ϕ , changes linearly with time, t . We ignore the changes in the poloidal magnetic field $\delta\vec{B}_p$, and in the relevant azimuthal current δj_ϕ . The early phase of the toroidal magnetic field is expressed as δB_ϕ and can be approximated as

$$\delta B_\phi = \frac{\delta S}{\varpi} \left(\frac{t}{\tau_H} \right), \quad (18)$$

where the function $\delta S(r, \theta)$ is explicitly expressed in terms of the Legendre polynomial $P_l(\cos \theta)$ of $l = 2$ as

$$\delta S \equiv y(r) \sin \theta P_{2,\theta} = \frac{2K_0\rho_c(\Delta r)^2}{3B_0} \hat{\chi}' g \sin \theta P_{2,\theta}, \quad (19)$$

where the radial function, y is defined for convenience. The poloidal current changes are associated with δB_ϕ ; thus, the Lorentz force, $\delta\vec{f} = c^{-1}(\delta\vec{j} \times \vec{B} + \vec{j} \times \delta\vec{B})$ also changes and is explicitly written as

$$\delta\vec{f} = -[\vec{\nabla}(S\delta S) + \vec{\nabla}\Psi \times \vec{\nabla}\delta S] \left(\frac{t}{4\pi\varpi^2\tau_H} \right). \quad (20)$$

2.4. Quasi-stationary Elastic Response

The force balance deviates slightly from the initial state owing to the change in the Lorentz force through magnetic field evolution. The acceleration associated with Equation (20) is generally the sum of the solenoidal and irrotational components. The solenoidal part of the Lorentz force should be balanced by additional forces when the material distribution is barotropic; that is, the sum of the pressure and gravitational potential terms is expressed as $-\vec{\nabla}\delta\Phi_{\text{eff}}$. The elastic force $\delta\vec{h}$ in the solid crust is assumed to act against the solenoidal part. Note that the force is purely solenoidal for incompressible motion in the case of a constant shear modulus μ ; that is, $\delta\vec{h} = -\mu\vec{\nabla} \times \vec{\nabla} \times \vec{\xi}$ with the displacement vector $\vec{\xi}$ (for example Landau & Lifshitz's 1959). In general, the force contains both solenoidal and irrotational parts, and is expressed by the trace-free strain tensors σ_{ij} and μ .

$$\delta h^i = \nabla_j (2\mu\sigma^{ij}) \quad (21)$$

and

$$\sigma_{ij} = \frac{1}{2}(\nabla_i\xi_j + \nabla_j\xi_i), \quad (22)$$

where the incompressible displacement is assumed as $\vec{\nabla} \cdot \vec{\xi} = 0$. In addition, we assumed that the shear modulus μ is proportional to the density (Figure 43 in [Chamel & Haensel 2008](#)), such that the shear speed v_s is constant throughout the crust and $\mu = v_s^2 \rho$, where

$$v_s = 8.5 \times 10^7 \text{ cm s}^{-1}. \quad (23)$$

The shear modulus μ is the maximum, $\mu_c \approx 10^{30} \text{ erg cm}^{-3}$ at the core–crust interface while it decreases toward the stellar surface, $\mu_1 \approx 3 \times 10^{27} \text{ erg cm}^{-3}$ at ρ_1 .

The elastic evolution was excessively slow; hence, the acceleration $\partial^2 \xi_i / \partial t^2$ can be ignored. Consequently, the elastic force is balanced by the change in the Lorentz force at any time, that is, quasi-stationary evolution. Under the approximation that the solenoidal part, that is, a "curl" of acceleration owing to the Lorentz force should be balanced with that of the elastic force, a set of equations is expressed as

$$(\delta \vec{f} + \delta \vec{h})_\phi = 0, \quad (24)$$

$$[\vec{\nabla} \times \rho^{-1}(\delta \vec{f} + \delta \vec{h})]_\phi = 0. \quad (25)$$

Note that we consider the azimuthal component only in Equation (25) because other poloidal components are redundant when using Equation (24) and an axial symmetry ($\partial_\phi = 0$). The terms involving the Lorentz force in Equations (24) and (25) are expressed in terms of Legendre polynomials $P_l(\cos \theta)$ of $l = 1, 3$ ¹.

$$\delta f_\phi = - \sum_{l=1,3} r^{-3} a_l P_{l,\theta} \left(\frac{t}{\tau_H} \right). \quad (26)$$

$$[\vec{\nabla} \times \rho^{-1} \delta \vec{f}]_\phi = - \sum_{l=1,3} r^{-1} b_l P_{l,\theta} \left(\frac{t}{\tau_H} \right). \quad (27)$$

where a_l and b_l ($l = 1, 3$) are radial functions expressed as

$$a_1 = -\frac{3}{10\pi}(gy)', \quad a_3 = -\frac{1}{10\pi}(2(gy)' - 5g'y), \quad (28)$$

$$b_1 = \frac{3\kappa}{10\pi} \frac{(gy)'}{\rho r^2}, \quad b_3 = \frac{\kappa}{10\pi} \left(\frac{2(gy)'}{\rho r^2} + 5 \left(\frac{1}{\rho r^2} \right)' gy \right). \quad (29)$$

The elastic displacement growth with t is explicitly expressed as

$$(\xi_r, \xi_\theta, \xi_\phi) = \sum_{l=1,3} \left(\frac{l(l+1)x_l}{r^2} P_l, \frac{x'_l}{r} P_{l,\theta}, -rk_l P_{l,\theta} \right) \left(\frac{t}{\tau_H} \right), \quad (30)$$

where the radial functions x_l and k_l ($l = 1, 3$) are determined using Equations (24) and (25) ([Kojima et al. 2022](#));

$$(\mu r^4 k'_l)' - (l-1)(l+2)\mu r^2 k_l = -a_l, \quad (31)$$

$$x''_l - \frac{l(l+1)}{r^2} x_l + \frac{1}{\mu} w_l = 0, \quad (32)$$

$$\left[\rho^{-1} w'_l + 2 \left(\frac{\mu'}{\rho r} \right) x'_l \right]' - \frac{l(l+1)}{r^2} \left[\rho^{-1} w'_l + 2 \left(\frac{\mu'}{\rho} \right)' x_l \right] = -b_l. \quad (33)$$

We now discuss the boundary conditions for a set of ordinary differential equations (31) - (33). Across these surfaces at r_c or R , the change in the total stress–tensor should vanish for force balance. In other words, $2\mu\sigma_{ri} + \delta T_{ri} = 0$ ($i = r, \theta, \phi$), where δT_{ij} denotes magnetic stress. Owing to the fact that $\delta \vec{B}_p = 0$ and $B_r = B_\phi = 0$ at the boundaries,

¹ Initial barotropic equilibrium models are magnetically deformed with an ellipticity (deformation of $l = 2$) $\sim 10^{-8}(B_0/(10^{14}\text{G}))^2$ (e.g., [Kojima et al. 2021](#)). The quadrupole deformation does not change because the induced components are $l = 1$ and 3.

the boundary conditions are reduced to $\sigma_{rr} = \sigma_{r\theta} = \sigma_{r\phi} = 0$. These conditions for the radial functions k_l , x_l and w_l ($l = 1, 3$) at r_c and R can be written explicitly as

$$rx'_l - 2x_l = 0, \quad (34)$$

$$2\mu r x'_l - 2\mu l(l+1)x_l + r^2 w_l = 0, \quad (35)$$

$$k'_l = 0. \quad (36)$$

3. RESULTS

3.1. Breakup Time and Accumulated Energy

By solving the differential equations, we obtain the shear stress σ_{ij} whose magnitude increases with time, whereas the spatial profile remains unchanged. The numerical calculations provided the maximum shear stress with respect to (r, θ) in the crust. Elastic equilibrium can be achieved until the breakup time t_* , only when the shear strain satisfies a particular criterion. We adopted the following (von Mises criterion) to determine the elastic limit:

$$\frac{1}{2}\sigma_{ij}\sigma^{ij} \leq (\sigma_{\max})^2, \quad (37)$$

where σ_{\max} denotes the number of $\sigma_{\max} \approx 10^{-2} - 10^{-1}$ (Horowitz & Kadau 2009; Caplan et al. 2018; Baiko & Chugunov 2018). Thus, the period of the elastic response is expressed as

$$t \leq t_* \equiv \hat{t}_b \left(\frac{\sigma_{\max}}{0.1} \right) \left(\frac{v_s}{v_a} \right)^2 \tau_H \quad (38)$$

$$= 2.8 \times 10^6 \times \hat{t}_b \left(\frac{\sigma_{\max}}{0.1} \right) \left(\frac{B_0}{10^{14}\text{G}} \right)^{-3} \text{ yr}, \quad (39)$$

where \hat{t}_b is a numerical factor that depends on parameter κ . The criterion in Equation (38) depends on the ratio of shear to magnetic forces, and is characterized by the shear speed v_s and Alfvén speed v_a , which is defined as

$$v_a = \frac{B_0}{\sqrt{4\pi\rho_1}} = 4.5 \times 10^7 \left(\frac{B_0}{10^{14}\text{G}} \right) \text{ cm s}^{-1}, \quad (40)$$

where B_0 is determined by the poloidal magnetic energy E_p as discussed in Subsection 2.1.

Figure 5 illustrates \hat{t}_b as a function of $\kappa\Delta r$. The value is typically $\hat{t}_b = 0.1 - 1$ except for sharp peaks at $\kappa\Delta r \approx n\pi$ ($n = 1, 2, 3, \dots$), which correspond to force-free cases with $K_0 \rightarrow 0$. It is interesting to compare the numbers $\hat{t}_b = 1.5 \times 10^{-3}$ for the dipolar magnetic-field extending to exterior vacuum for the same E_p (Paper I). The breakup time for the confined field was significantly longer. This difference is related to the spatial shear distribution driven by the magnetic-field geometry. This will be discussed in the next subsection.

The elastic energy ΔE_{elas} increased with the square of time t . We numerically integrated over the entire crust and obtained

$$\begin{aligned} \Delta E_{\text{elas}} &= 2\pi \int_{r_c}^R r^2 dr \int_0^\pi \sin\theta d\theta \mu \sigma_{ij} \sigma^{ij} \\ &= \hat{E}_{\text{elas}} \times \mu_1 R^3 \left(\frac{\sigma_{\max}}{0.1} \right)^2 \left(\frac{t}{t_*} \right)^2, \end{aligned} \quad (41)$$

where \hat{E}_{elas} is the numerical value, and ΔE_{elas} was normalized by $\mu_1 R^3 = 5.0 \times 10^{45}$ erg using μ_1 at ρ_1 .

The change in magnetic energy ΔE_{mag} associated with δB_ϕ is expressed as

$$\begin{aligned} \Delta E_{\text{mag}} &= 2\pi \int_{r_c}^R r^2 dr \int_0^\pi \sin\theta d\theta \frac{(\delta B_\phi)^2}{8\pi} \\ &= \hat{E}_{\text{mag}} \times E_p \left(\frac{\sigma_{\max}}{0.1} \right)^2 \left(\frac{v_s}{v_a} \right)^4 \left(\frac{t}{t_*} \right)^2, \end{aligned} \quad (42)$$

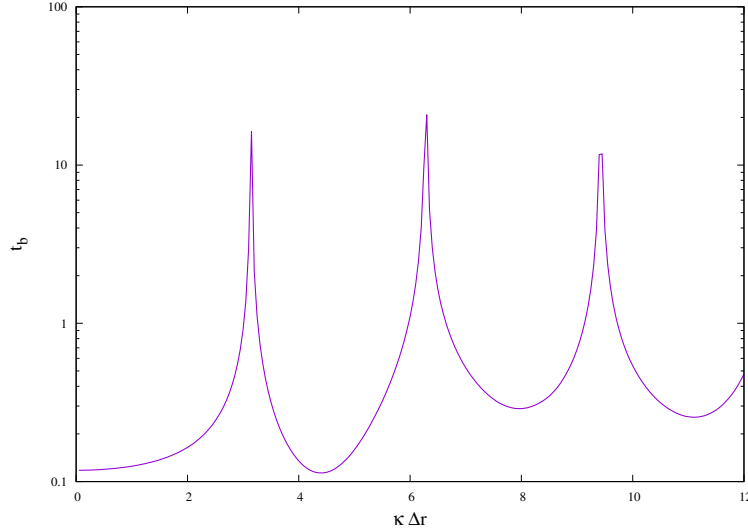


Figure 5. Breakup-time \hat{t}_b as a function of $\kappa\Delta r$.

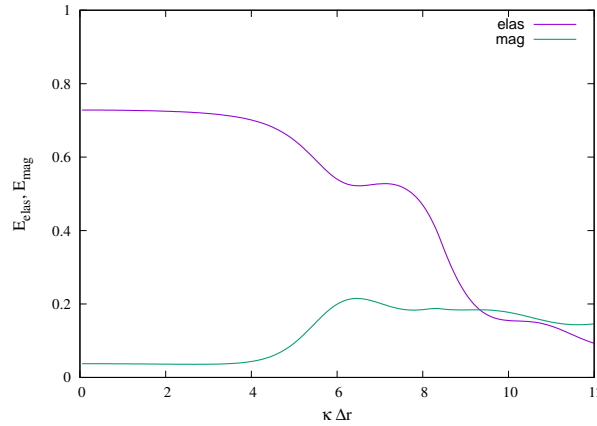


Figure 6. Coefficients \hat{E}_{elas} and \hat{E}_{mag} as a function of $\kappa\Delta r$.

where \hat{E}_{mag} is the numerical value. The poloidal magnetic energy $E_p = 4 \times 10^{46} (B_0/10^{14} \text{G})^2$ erg was chosen as the normalization, and other factors were derived using t_* . Both \hat{E}_{elas} and \hat{E}_{mag} are shown in Figure 6 as a function of $\kappa\Delta r$. The numerical factor \hat{E}_{elas} decreased, whereas \hat{E}_{mag} increased. The change with respect to $\kappa\Delta r$ was not large and \hat{E}_{elas} and \hat{E}_{mag} were $\mathcal{O}(1)$ for all models.

Numerical coefficients in front of Equations (38), (41), and (42) and t_d/τ_{Ohm} are summarized in Table 1. These numbers were also compared with those in Paper I. A significant difference was observed in the magnetic configuration. The breakup time for the confined model was typically 10^2 times longer than that for the extended model. This longer timescale led to higher energies \hat{E}_{elas} and \hat{E}_{mag} , which typically increased by a factor of 10^4 corresponding to the square of accumulation time. However, longer timescale constrained the epoch or magnetic field strength because the ohmic decay was neglected. The condition under which $t_* \leq t_d$ is $B_0 \geq 3.2 \times 10^{13} (\sigma_{\text{max}}/0.1)^{1/3}$ G for the extended model. However, lower field strength increased by a factor of 5 for the confined model; $B_0 \geq 1.6 \times 10^{14} (\sigma_{\text{max}}/0.1)^{1/3}$ G at least.

3.2. Spatial Shear-Distribution

Figure 7 shows the magnitude of shear $\sigma \equiv (\sigma_{ij}\sigma^{ij}/2)^{1/2}$ in the crust. We found that the shear associated with the axial displacement ξ_ϕ was significantly larger than that of the polar displacement $\vec{\xi}_p = (\xi_r, \xi_\theta)$. This is related to the thin crust of thickness $\Delta r/R = 0.05$; typically, $|\xi_p| \sim \Delta r/R \times |\xi_\phi|$. Polar displacement $\vec{\xi}_p$ was induced only when the

Model	Figure	t_d/τ_{Ohm}	$\hat{t}_b (t_*)$	\hat{E}_{elas}	\hat{E}_{mag}
Extending to exterior	Figure 1-a	5.9×10^{-2}	1.5×10^{-3}	2.0×10^{-4}	5.3×10^{-5}
Confined to interior and Figure 1-c	$3 \times 10^{-3} - 3 \times 10^{-2}$	0.1 – 10	0.1 – 0.8	0.1 – 0.2	

Table 1. Numerical values for magnetic decay time (11), breakup time(38), elastic energy(41), and magnetic energy(42)

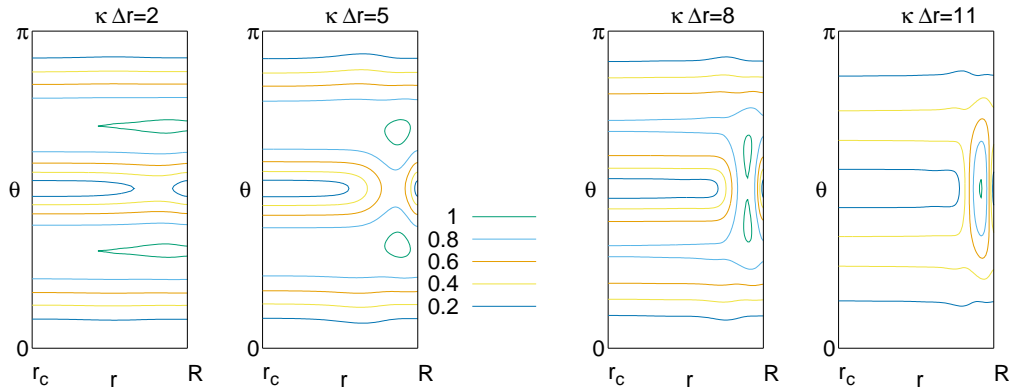


Figure 7. Contour map of the magnitude σ of shear stress normalized by the maximum value. The left to right panels show the results for the models with $\kappa\Delta r = 2, 5, 8,$ and 11.

initial MHD equilibrium contained the toroidal component of the magnetic field ($b_l \neq 0$ for $\kappa \neq 0$ in Equation (29)). However, the shear distribution shown in Figure 7 was almost the same when changing κ , which determined the ratio of the toroidal to poloidal components of magnetic field. The maximum position of σ shifted slightly to the outer radius with increasing radial nodes.

The question that arises is where is the origin of the significant difference, for example, in the breakup time between the extending model and the confined models. The initial equilibrium for the former considered in Paper I was purely poloidal. In contrast to the shear distribution shown in Figure 7, σ exhibited a sharp peak at the surface at $\pm \cos^{-1}(1/\sqrt{3})$ for the extended model (see Figure 2 in Paper I). The peak originated from the acceleration $a_\theta \neq 0$ on the surface of the extended model. In contrast, $a_\theta = 0$ because of $\Psi = 0$ at the surface of the confined model (Equation (5)). The surface was very fragile because of its weak shear-modulus. This region was avoided in the confined model, such that the breakup time to the elastic limit increased.

4. DISCUSSION

We considered the elastic deformation induced by the evolution of a magnetic field. The effect of magnetic field geometry was studied and compared with the results of Paper I. When the field was confined to the interior, the breakup time for the elastic limit increased by a factor of 10^2 compared with a field extending to the exterior with the same magnetic energy. Accordingly, a larger elastic energy was deposited until crustal fracture. The elastic energy was typically $\sim 10^{45}$ erg. The accumulated energy was dependent on the magnetic field geometry and independent of

the strength B_0 . Breakup time t_* was proportional to B_0^{-3} ; $t_* \sim 10^5(\sigma_{\max}/0.1)(B_0/(10^{14}\text{G}))^{-3}$ years. As the Ohmic decay of the magnetic field was neglected, our result is valid for stronger field, $B_0 \geq 2 \times 10^{14}(\sigma_{\max}/0.1)^{1/3}$ G at least. Further, the average strength exceeded $2 \times 10^{15}(\sigma_{\max}/0.1)^{1/3}$ G. The magnetic energy in the crust exceeded 2×10^{47} erg and the breakup time corresponding to the minimum strength was $\sim 10^4$ year. Unless the field strength B_0 was significantly larger than 2×10^{14} G, the elastic deformation did not reach the critical limit. The magnetic field in CCOs may be stable and gradually decays owing to the Joule loss.

Our magnetic configuration is limited to a simple case that is, it has a dipolar angular configuration and a few radial nodes. The elastic limit in a more general configuration is worth discussing based on the results of this study because a realistic magnetic field in CCOs is more complicated.

When the number of nodes increases in either the angular or radial direction, spatial size around the maximum shear strain decreases. The elastic energy was deposited until the critical limit decreased. Assuming that the accumulated elastic energy is released during an outburst, such an event is less energetic. Thus, the number of radial nodes may be effective, because the stellar structure changed significantly in the radial direction, and the outer part near the surface was more prone to breaking. Simultaneously, ohmic dissipation became effective near the surface. Therefore, it would be interesting to investigate whether a small-scale irregularity in the magnetic field leads to elastic limit or decay.

However, in the highly tangled limit, the magnetic field was irregular on a small scale and the direction was random. Thus, the magnetic force can be regarded as isotropic magnetic pressure, which causes irrotational force. It is difficult to drive elastic deformation; thus, the confined field was stable against elastic fractures.

A strong magnetic field in CCOs is hidden in the crust and is unlikely to lead to outbursts that occur in magnetars, although the field strength in both sources is of the same order. The field geometry exhibits a remarkable difference. Observations of burst events were not reported, except for CCO at RCW 103. Further, the central neutron star was classified as a magnetar with spin period ~ 6.7 h (D’Ai et al. 2016). Future studies will be conducted to examine a simple idea of different field geometries resulting in the occurrence or absence of outburst in strongly magnetized neutron stars.

ACKNOWLEDGEMENTS

This work was supported by JSPS KAKENHI Grant Numbers JP17H06361, JP19K03850(YK), JP19K14712, JP21H01078, JP22H01267, JP22K03681(SK), JP20H04728(KF).

REFERENCES

- Baiko, D. A., & Chugunov, A. I. 2018, MNRAS, 480, 5511, doi: [10.1093/mnras/sty2259](https://doi.org/10.1093/mnras/sty2259)
- Caplan, M. E., Schneider, A. S., & Horowitz, C. J. 2018, PhRvL, 121, 132701, doi: [10.1103/PhysRevLett.121.132701](https://doi.org/10.1103/PhysRevLett.121.132701)
- Chamel, N., & Haensel, P. 2008, Living Reviews in Relativity, 11, 10, doi: [10.12942/lrr-2008-10](https://doi.org/10.12942/lrr-2008-10)
- D’Ai, A., Evans, P. A., Burrows, D. N., et al. 2016, MNRAS, 463, 2394, doi: [10.1093/mnras/stw202310.48550/arXiv.1607.04264](https://doi.org/10.1093/mnras/stw202310.48550/arXiv.1607.04264)
- De Grandis, D., Turolla, R., Wood, T. S., et al. 2020, ApJ, 903, 40, doi: [10.3847/1538-4357/abb6f9](https://doi.org/10.3847/1538-4357/abb6f9)
- Douchin, F., & Haensel, P. 2001, A&A, 380, 151, doi: [10.1051/0004-6361:20011402](https://doi.org/10.1051/0004-6361:20011402)
- Duncan, R. C., & Thompson, C. 1992, ApJL, 392, L9, doi: [10.1086/186413](https://doi.org/10.1086/186413)
- Enoto, T., Kisaka, S., & Shibata, S. 2019, Reports on Progress in Physics, 82, 106901, doi: [10.1088/1361-6633/ab3def](https://doi.org/10.1088/1361-6633/ab3def)
- Esposito, P., Rea, N., & Israel, G. L. 2021, in Astrophysics and Space Science Library, Vol. 461, Astrophysics and Space Science Library, ed. T. M. Belloni, M. Méndez, & C. Zhang, 97–142, doi: [10.1007/978-3-662-62110-3_3](https://doi.org/10.1007/978-3-662-62110-3_3)
- Fujisawa, K., & Eriguchi, Y. 2013, MNRAS, 432, 1245, doi: [10.1093/mnras/stt541](https://doi.org/10.1093/mnras/stt541)
- Fujisawa, K., Kojima, Y., & Kisaka, S. 2023, MNRAS, 519, 3776, doi: [10.1093/mnras/stac375010.48550/arXiv.2212.08309](https://doi.org/10.1093/mnras/stac375010.48550/arXiv.2212.08309)
- Gotthelf, E. V., Halpern, J. P., & Alford, J. 2013, ApJ, 765, 58, doi: [10.1088/0004-637X/765/1/58](https://doi.org/10.1088/0004-637X/765/1/58)
- Gotthelf, E. V., Perna, R., & Halpern, J. P. 2010, ApJ, 724, 1316, doi: [10.1088/0004-637X/724/2/1316](https://doi.org/10.1088/0004-637X/724/2/1316)
- Gourgouliatos, K. N., & Cumming, A. 2014, MNRAS, 438, 1618, doi: [10.1093/mnras/stt2300](https://doi.org/10.1093/mnras/stt2300)
- Gourgouliatos, K. N., Cumming, A., Reisenegger, A., et al. 2013, MNRAS, 434, 2480, doi: [10.1093/mnras/stt1195](https://doi.org/10.1093/mnras/stt1195)
- Gourgouliatos, K. N., Hollerbach, R., & Igoshev, A. P. 2020, MNRAS, 495, 1692, doi: [10.1093/mnras/staa1295](https://doi.org/10.1093/mnras/staa1295)

- Gourgouliatos, K. N., & Lander, S. K. 2021, MNRAS, 506, 3578, doi: [10.1093/mnras/stab1869](https://doi.org/10.1093/mnras/stab1869)
- Ho, W. C. G. 2011, MNRAS, 414, 2567, doi: [10.1111/j.1365-2966.2011.18576.x](https://doi.org/10.1111/j.1365-2966.2011.18576.x)
- Horowitz, C. J., & Kadau, K. 2009, PhRvL, 102, 191102, doi: [10.1103/PhysRevLett.102.191102](https://doi.org/10.1103/PhysRevLett.102.191102)
- Igoshev, A. P., Gourgouliatos, K. N., Hollerbach, R., & Wood, T. S. 2021, ApJ, 909, 101, doi: [10.3847/1538-4357/abde3e](https://doi.org/10.3847/1538-4357/abde3e)
- Kaspi, V. M., & Beloborodov, A. M. 2017, ARA&A, 55, 261, doi: [10.1146/annurev-astro-081915-023329](https://doi.org/10.1146/annurev-astro-081915-023329)
- Kojima, Y. 2022, ApJ, 938, 91, doi: [10.3847/1538-4357/ac9184](https://doi.org/10.3847/1538-4357/ac9184)
- Kojima, Y., & Kisaka, S. 2012, MNRAS, 421, 2722, doi: [10.1111/j.1365-2966.2012.20509.x](https://doi.org/10.1111/j.1365-2966.2012.20509.x)
- Kojima, Y., Kisaka, S., & Fujisawa, K. 2021, MNRAS, 506, 3936, doi: [10.1093/mnras/stab1848](https://doi.org/10.1093/mnras/stab1848)
- . 2022, MNRAS, 511, 480, doi: [10.1093/mnras/stac036](https://doi.org/10.1093/mnras/stac036)
- Kojima, Y., & Suzuki, K. 2020, MNRAS, 494, 3790, doi: [10.1093/mnras/staa1045](https://doi.org/10.1093/mnras/staa1045)
- Landau, L. D., & Lifshitz, E. M. 1959, Theory of elasticity (Pergamon Press, London)
- Lander, S. K. 2016, ApJ, 824, L21, doi: [10.3847/2041-8205/824/2/L21](https://doi.org/10.3847/2041-8205/824/2/L21)
- Lander, S. K., & Gourgouliatos, K. N. 2019, MNRAS, 486, 4130, doi: [10.1093/mnras/stz1042](https://doi.org/10.1093/mnras/stz1042)
- Li, X., Levin, Y., & Beloborodov, A. M. 2016, ApJ, 833, 189, doi: [10.3847/1538-4357/833/2/189](https://doi.org/10.3847/1538-4357/833/2/189)
- Matsumoto, J., Asahina, Y., Takiwaki, T., Kotake, K., & Takahashi, H. R. 2022, MNRAS, 516, 1752, doi: [10.1093/mnras/stac2335](https://doi.org/10.1093/mnras/stac2335)
- Pons, J. A., & Geppert, U. 2007, A&A, 470, 303, doi: [10.1051/0004-6361:20077456](https://doi.org/10.1051/0004-6361:20077456)
- Shabaltas, N., & Lai, D. 2012, ApJ, 748, 148, doi: [10.1088/0004-637X/748/2/148](https://doi.org/10.1088/0004-637X/748/2/148)
- Suvorov, A. G., & Kokkotas, K. D. 2019, MNRAS, 488, 5887, doi: [10.1093/mnras/stz2052](https://doi.org/10.1093/mnras/stz2052)
- Thompson, C., & Duncan, R. C. 1995, MNRAS, 275, 255, doi: [10.1093/mnras/275.2.255](https://doi.org/10.1093/mnras/275.2.255)
- Tomimura, Y., & Eriguchi, Y. 2005, MNRAS, 359, 1117, doi: [10.1111/j.1365-2966.2005.08967.x](https://doi.org/10.1111/j.1365-2966.2005.08967.x)
- Turolla, R., Zane, S., & Watts, A. L. 2015, Reports on Progress in Physics, 78, 116901, doi: [10.1088/0034-4885/78/11/116901](https://doi.org/10.1088/0034-4885/78/11/116901)
- Viganò, D., Garcia-Garcia, A., Pons, J. A., Dehman, C., & Graber, V. 2021, Computer Physics Communications, 265, 108001, doi: [10.1016/j.cpc.2021.108001](https://doi.org/10.1016/j.cpc.2021.108001)
- Viganò, D., & Pons, J. A. 2012, MNRAS, 425, 2487, doi: [10.1111/j.1365-2966.2012.21679.x](https://doi.org/10.1111/j.1365-2966.2012.21679.x)
- Viganò, D., Rea, N., Pons, J. A., et al. 2013, MNRAS, 434, 123, doi: [10.1093/mnras/stt1008](https://doi.org/10.1093/mnras/stt1008)
- Viganò, D., Martínez-Gómez, D., Pons, J. A., et al. 2019, Computer Physics Communications, 237, 168, doi: [10.1016/j.cpc.2018.11.022](https://doi.org/10.1016/j.cpc.2018.11.022)
- Wood, T. S., & Hollerbach, R. 2015, PhRvL, 114, 191101, doi: [10.1103/PhysRevLett.114.191101](https://doi.org/10.1103/PhysRevLett.114.191101)